MRI INDUCED HEATING OF DEEP BRAIN STIMULATION LEADS: EFFECT OF THE AIR-TISSUE INTERFACE

S. A. Mohsin and N. M. Sheikh

Department of Electrical Engineering
University of Engineering and Technology
Lahore, Pakistan

U. Saeed

School of Electrical and Computer Engineering
Georgia Institute of Technology
Atlanta, GA, USA

Abstract—We have investigated the scattering of the Magnetic Resonance Imaging (MRI) radiofrequency (RF) field by implants for Deep Brain Stimulation (DBS) and the resultant heating of the tissue surrounding the DBS electrodes. The finite element method has been used to perform full 3-D realistic simulations. The near field has been computed for varying distances of the connecting portion of the lead from the air-tissue interface. Dissipated powers and induced temperature rise distributions have been obtained in the region surrounding the electrodes. It is shown that the near proximity of the air-tissue interface results in a reduction in the induced temperature rise.

1. INTRODUCTION

Deep brain stimulation (DBS) systems are being increasingly used in the treatment of neurological disorders such as Parkinson's disease. Figure 1 illustrates the use of such systems in which an implantable pulse generator (IPG) is connected to DBS electrodes for the chronic stimulation of the thalamus, global pallidus, or subthalamic nucleus [1]. The connecting part of the lead runs just below the skin and consists of thin individually insulated wires contained in an insulating sheath. The DBS electrodes are placed optimally inside the brain under MRI guidance, and often post-implantation MRI procedures need to be
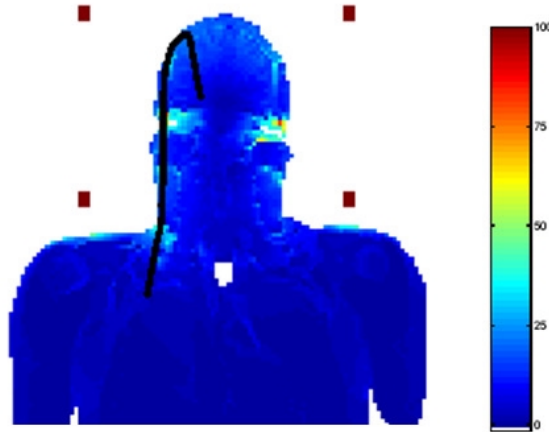
Figure 1. The use of a lead for neurostimulation. The shading shows the electric intensity in V/m of the typical background RF field (*without* an implant) that exists in tissue. The lead is shown to illustrate its placement. The scattered field of the lead is *not* shown in this figure.

performed [1, 2]. This necessitates an investigation into the interaction of the MRI fields with the DBS lead implant.

In a typical whole-body cylindrical bore MRI system, there are three types of fields. These are a static magnetic field B_0 which is typically 1.5 or 3.0 Tesla, pulsed gradient fields which are magnetic field pulses with spatial variations, and an RF electromagnetic field B_1 [3, 4]. The static magnetic field does not interact with the DBS lead. This is due to the fact that no magnetic materials are present and there is no direct current. The pulsed gradient fields induce currents in body tissue and a long wire implant has a concentrating effect on these currents. However this concentration tends to be small due to cancellation effects of the surrounding tissue [3]. The strongest interaction with the lead is shown by the MRI RF field that exists inside body tissues; this is due to the fact that this field is scattered by the lead structure.

The frequency of the B_1 RF field is determined from the strength of the B_0 field. The Larmor frequency is 42.58 MHz/T, and for a 1.5 T system the frequency of the B_1 field will be 42.58 MHz×1.5 = 63.86 MHz. A typical DBS lead implant has an overall length in the range 20 to 50 cm. At 63.86 MHz the wavelength of the B_1 field in air, λ_{air}, is 4.7 m and that in typical body tissue, $\lambda_{\mathrm{tissue}}$, with conductivity 0.27 S/m and relative permittivity 77, is 0.488 m. For

this wavelength of the MRI RF field in tissue, there will be a strong coupling of this field with the implanted DBS lead device. In fact the long conducting wires connecting the IPG to the DBS electrodes will show waveguide properties which will produce very intense fields at the tips of the lead [5]. The MRI RF field in a patient's body without an implant has been the subject of a number of research studies [4, 6]. The effect of a DBS lead implant is of course to further concentrate this RF field in the immediate region around the implant, especially at the tips. In terms of electromagnetic behavior, a DBS lead embedded within body tissue is like an antenna in a dissipative medium. King et al. [7–9] analyzed such antennas using transmission line theory to find the current in the antenna and then the radiation integrals were used to obtain the surrounding fields. Atlamazoglou et al. [10] applied the method of moments (MoM) to an insulated antenna in a homogeneous and infinite dissipative medium. Park et al. [11] applied the method in [10] to find the scattered field due to a DBS lead using the homogeneous and infinite medium idealization. In actual practice, the lead runs close to the skin for most of its length and only the last few centimeters are embedded deep inside brain tissue. Also the tissue containing the lead is not homogeneous; the constitutive parameters of brain tissue are different from those of the tissue adjacent to the skin which has a greater fat content. The present paper takes into account the proximity of the lead to the air-tissue interface as well as the inhomogeneous nature of the tissue in which the lead is embedded. It is shown in the present paper that the scattered field decays to almost zero within a radial distance of about 2.5 cm from the lead axis. The finite-element-method is used to find the scattered field as it is mathematically well-suited to handle the inhomogeneous nature of the computational domain as compared to the moment method [12]. Finally the Pennes' bioheat equation is solved to find the temperature rise in the brain tissue surrounding the electrodes.

2. COMPUTATION OF THE SCATTERED FIELD

Figure 2 shows the model lead structure. Let $(\mathbf{E}^i, \mathbf{H}^i)$ be the incident electromagnetic field satisfying the free-space Maxwell's equations. This incident field excites a finite region of space occupied by a medium having conductivity σ and permittivity ε. No magnetic media are present and thus the permeability is always equal to μ_0. From Maxwell's equations we find that the scattered field $(\mathbf{E}^s, \mathbf{H}^s)$ inside

the finite region then must satisfy

$$\nabla \times \mathbf{H}^s = (\sigma + j\omega\varepsilon)\,\mathbf{E}^s + \mathbf{J}^i \tag{1}$$

$$\nabla \times \mathbf{E}^s = -j\omega\mu_0\mathbf{H}^s \tag{2}$$

where $\mathbf{J}^i = \{\sigma + j\omega\,(\varepsilon - \varepsilon_0)\}\,\mathbf{E}^i$, and ω is the angular frequency. The conductivity σ and permittivity $\varepsilon = \varepsilon_0\varepsilon_r$ of the media occupying the different regions are specified in Figure 2. Inserting in (1) and (2) the proper values of σ and ε for each region gives the equations describing the scattered field $(\mathbf{E}^s, \mathbf{H}^s)$ in that region. Taking the curl of (2) and using (1) leads to the equation

$$(1/j\omega\mu_0)\,\nabla \times \nabla \times \mathbf{E}^s = -\mathbf{J}^i - (\sigma + j\omega\varepsilon)\,\mathbf{E}^s \tag{3}$$

Weighting with a set of real vector functions $\mathbf{v(r)}$, where $\mathbf{r}$ is the position vector, and integrating over the entire volume V of the computational domain we have

$$\int_V \left[\left(\frac{1}{j\omega\mu_0}\right)\nabla\times\nabla\times\mathbf{E}^s \cdot \mathbf{v(r)} + (\sigma + j\omega\varepsilon)\mathbf{E}^s\cdot\mathbf{v(r)}\right]dV = -\int_V \mathbf{J}^i \cdot \mathbf{v(r)}dV \tag{4}$$

The components of $\mathbf{v(r)}$ must be square integrable. Using Green's
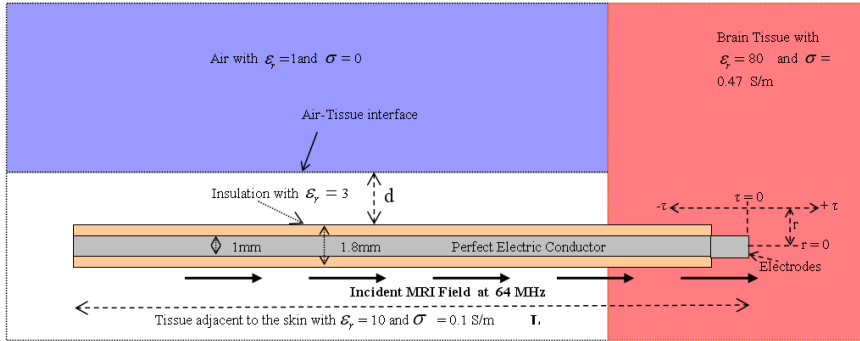
Figure 2. A cross-section of the computational domain is shown. $L = 25$ or $48\,\mathrm{cm}$ and $d = 3, 9,$ or $15\,\mathrm{mm}$. The background SAR values are as follows: In fat tissue: $0.5\,\mathrm{W/kg}$: in brain tissue: $2.35\,\mathrm{W/kg}$. The cross-sectional plane shown passes through the central axis of the implanted lead and is perpendicular to the air-tissue interface. The figure is not drawn to scale (since $L \gg$ lead dia).

first vector identity we are led to the weak form

$$\int_V \left[\frac{1}{j\omega\mu_0} (\nabla \times \mathbf{E}^s) \cdot (\nabla \times \mathbf{v}(\mathbf{r})) + (\sigma + j\omega\varepsilon) \mathbf{E}^s \cdot \mathbf{v}(\mathbf{r}) \right] dV$$

$$- \int_S \hat{n} \times \mathbf{H}^s \cdot \mathbf{v}(\mathbf{r}) dS = - \int_V \mathbf{J}^i \cdot \mathbf{v}(\mathbf{r}) dV \tag{5}$$

At the exterior bounding surface S, $\mathbf{H}^s$ can be related to $\mathbf{E}^s$ by a second-order absorbing boundary condition (ABC) [12],

$$\hat{n} \times \mathbf{H}^s = -\sqrt{\frac{\varepsilon_0}{\mu_0}} \mathbf{E}^s_t + \frac{j}{2(\omega\mu_0)^2} \sqrt{\frac{\mu_0}{\varepsilon_0}} \left[\nabla \times (\hat{n}(\nabla \times \mathbf{E}^s)_n) + \nabla_t (\nabla \cdot \mathbf{E}^s_t) \right] \tag{6}$$

where $\hat{n}$ is the outward unit normal to S and the subscripts t and n refer to the tangential and normal components to S respectively.

The volume V is divided into a number of volume elements. The whole computational domain in each of the different models solved here contains about 2×10^5 elements. We have used tetrahedral elements of unequal size. Regions where finer resolution is required contain more elements per unit volume than other regions. Here the lead region and the tissue near to and surrounding the lead are meshed much more finely than outlying tissue and the air region. The lead region (lead connecting portion, insulation, and electrodes) contains no less than 8×10^4 volume elements. The scattered field $\mathbf{E}^s$ is represented by an expansion (quadratic) of vector basis functions $\mathbf{w}(\mathbf{r})$ in each volume element V^e,

$$\mathbf{E}^\mathbf{s}(\mathbf{r}) = \sum_{p=1}^{N^e} E_p \mathbf{w}_p(\mathbf{r}) \tag{7}$$

where $N^e = 6$ is the number of edges in a tetrahedron. The $\mathbf{w}_p(\mathbf{r})$ are known as edge-base functions and are of the form as given in [12] and [13]. Each $\mathbf{w}_p(\mathbf{r})$ is nonzero if $\mathbf{r} \in V^e$ and zero otherwise. The E_p are unknown coefficients and are complex scalars. Substituting (6) in (5), and using (7) with Galerkin's testing, $\mathbf{v}(\mathbf{r}) = \mathbf{w}(\mathbf{r})$, we obtain the discretized form of (5) as

$$[A]\{E\} + [B]\{E\} = \{C^i\} \tag{8}$$

where

$$A_{mp}=\int\limits_V \left[\frac{1}{j\omega\mu_0}(\nabla\times\mathbf{w}_p(\mathbf{r}))\cdot(\nabla\times\mathbf{w}_m(\mathbf{r}))+(\sigma+j\omega\varepsilon)\mathbf{w}_p(\mathbf{r})\cdot\mathbf{w}_m(\mathbf{r})\right]dv \quad (9)$$

$$B_{mp}=\int\limits_S \left[\sqrt{\frac{\varepsilon_0}{\mu_0}}\mathbf{w}_{pt}(\mathbf{r}) - \frac{j}{2(\omega\mu_0)^2}\sqrt{\frac{\mu_0}{\varepsilon_0}}\left\{\nabla\times\left(\hat{n}\left(\nabla\times\mathbf{w}_p(\mathbf{r})\right)_n\right)\right.\right.$$

$$\left.\left.+\nabla_t\left(\nabla\cdot\mathbf{w}_{pt}(\mathbf{r})\right)\right\}\right]\cdot\mathbf{w}_m(\mathbf{r})dS \quad (10)$$

$$C_m^i = -\int\limits_V \mathbf{J}^i\cdot\mathbf{w}_m(\mathbf{r})dV \quad (11)$$

[A] is a sparse, banded, and symmetric $N\times N$ matrix. N is the total number of edges. [B] is a $N\times N$ sparse matrix with only those elements being nonzero that correspond to edges lying on S. {E} is a $N\times 1$ matrix of the unknown coefficients that are to be determined. $\{C^i\}$ is a known $N\times 1$ matrix. p and m are indices stepping through the N edges and the subscripts t and n mean tangential and normal, respectively (to S).

All DBS lead models, M_1 thru M_8, are as shown in Figure 2 and are described in Table 1.

Table 1. Description of DBS lead models. The lead geometry and the nature of the embedding tissue is as shown in Figure 2. All models are analyzed for a 1.5 Tesla MR system. L is the total length of the lead including the length of the electrodes.

M_1: $L = 25$ cm with no air-tissue interface ($d \to \infty$)	M_5: $L = 48$ cm with no air-tissue interface ($d \to \infty$)
M_2: $L = 25$ cm, $d = 15$ mm	M_6: $L = 48$ cm, $d = 15$ mm
M_3: $L = 25$ cm, $d = 9$ mm	M_7: $L = 48$ cm, $d = 9$ mm
M_4: $L = 25$ cm, $d = 3$ mm	M_8: $L = 48$ cm, $d = 3$ mm

3. SAR DISTRIBUTIONS AND DISSIPATED POWERS

The specific absorption rate (SAR in W/kg) is given by

$$\text{SAR} = \sigma\mathbf{E}\cdot\mathbf{E}^*/(2\rho) \quad (12)$$

where $\mathbf{E}^*$ is the conjugate of $\mathbf{E}$, σ is the conductivity, and ρ is the mass density of tissue. SAR is the absorbed power per unit mass at

a point and provides a good measure for the local resistive heating. The maximum SAR values at a lateral distance of 0.5 mm from the electrodes surface are found to be 8.21×10^3 W/kg and 3.46×10^4 W/kg for lead models M_1 and M_5 respectively. These are very high localized SAR values and are much greater than the SAR values produced inside head tissue due to mobile phones where the spatial peak values do not exceed 55 W/kg [15–18]. The quantity $(1/2)\sigma \mathbf{E} \cdot \mathbf{E}^*$ is integrated over the cylindrical volume $0 < r < 1$ cm, -2 cm $< \tau < 1$ cm for P_1, and over $0 < r < 0.5$ cm, -1 cm $< \tau < 0.5$ cm for P_2. The values of P_1 and P_2 are given in Table 2. Note that the electrode region is from $\tau = -6$ mm to $\tau = 0$. It is apparent from the values of the ratio P_2/P_1 that almost 87% of the power is dissipated (as heat) within a radial distance of 5 mm from the electrode surface.

Table 2. Dissipated powers.

DBS Lead	P_1 (mW)	P_2 (mW)	P_2/P_1 (%)	DBS Lead	P_1 (mW)	P_2 (mW)	P_2/P_1 (%)
M_1	525	460	87.6	M_5	2106	1839	87.3
M_2	502	440	87.7	M_6	1982	1731	87.3
M_3	480	420	87.5	M_7	1955	1707	87.3
M_4	425	372	87.5	M_8	1869	1633	87.4

4. INDUCED TEMPERATURE RISES

The temperature rise is found by solving the Pennes' bioheat equation,

$$\rho C_p \frac{\partial T}{\partial t} = \nabla (k \nabla T) - b (T - T_b) + Q \qquad (13)$$

where T is the temperature (°C) at a point at time t, ρ is the density (kg·m^{-3}) of the medium, C_p is the heat capacity (J·kg^{-1}°C^{-1}), k is the thermal conductivity (W·m^{-1}°C^{-1}), b is the blood perfusion constant, T_b is the blood temperature, and Q is the heat source (W·m^{-3}) at the point. We have $Q = \sigma \mathbf{E} \cdot \mathbf{E}^*/2$ at a point and $Q = \rho \cdot$ SAR in tissue. The effect of blood perfusion is to spread the temperature rise over a larger region of tissue. To investigate the worst case scenario for localized SAR heating over small tissue regions we take $b = 0$. An FEM tool was used to solve the bioheat equation. The thermal properties given in Table 3 were used. The induced temperature rises versus time are shown in Figure 3. The spatial temperature rise and

Table 3. Thermal properties of tissue and DBS lead materials.

Material	ρ (kg·m^{-3})	C_p (J·kg$^{-1\circ}$C^{-1})	k (W·m$^{-1\circ}$C^{-1})
Tissue	1000	4186	0.6
Insulation	1000	1500	0.2
Metal	8920	300	400
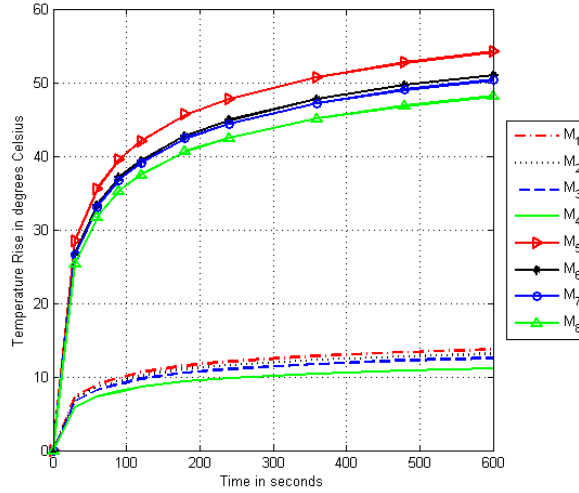
Figure 3. Temperature rise versus time plots. The plots are at the point $r = 1$ mm, $\tau = 0$.

the (corresponding) electric field distributions for a selected lead model are shown in Figure 4.

The proximity of the air-tissue interface to a DBS lead results in a slight decrease in the power dissipated in the tissue surrounding the electrodes as is evident from Table 2. M_1, with no air-tissue interface effect, is compared to M_2, M_3, and M_4 with $d = 15$, 9, and 3 mm respectively. Similarly M_5 is compared to M_6, M_7, and M_8. Figure 3 shows a comparison of the temperature rises for these lead models. It is apparent that as d will increase to 2 cm, the air-tissue interface effect will become almost negligible. Thus the infinite medium assumption is valid if the implant is embedded inside body tissue such that it is about 2 cm or more from the air-tissue interface. In-vitro temperature rise measurements have been made in a phantom of gelled material enclosed

in a MRI RF birdcage coil as detailed in [14]; these measurements were made with the lead well inside the phantom (far from the walls) and thus the infinite medium assumption is applicable. Our computed temperature rises for the infinite medium cases ($d \to \infty$) agree well with the in-vitro measurements.
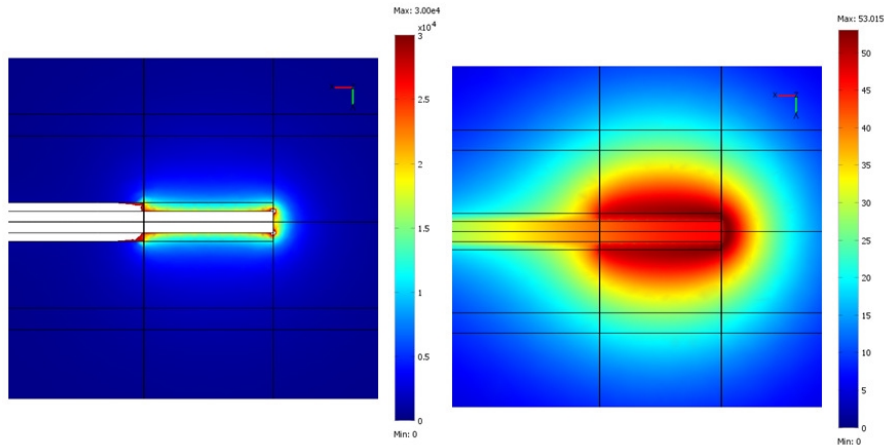
Figure 4. Figure showing the typical spatial distribution of the electric field (V/m) and the induced temperature rise (degrees Celsius) in brain tissue surrounding the electrodes. The plots are for lead model M_5. The temperature rise is shown after 6 minutes of application of RF input power.

5. CONCLUSIONS

Of the three fields used in MRI, only the RF field strongly interacts with a DBS lead. The interaction produces a very intense scattered field in the tissue surrounding the DBS electrodes. Conduction currents in the tissue cause heating and temperature rises as high as 53°C can result in the immediate proximity of the electrodes. The effect of the air-tissue interface is to decrease the intensity of the scattered field and hence to reduce the induced temperature rise as well. The effect of the air-tissue interface becomes negligible as the lateral distance of the interface from the lead increases to 2 cm or more.

ACKNOWLEDGMENT

REFERENCES

1. Rezai, A. R., D. Finneli, J. A. Nyenhuis, G. Hrdlicka, J. Tkach, A. Sharan, P. Rugieri, et al., "Neurostimulation systems for deep brain stimulation: In vitro evaluation of magnetic resonance imaging-related heating at 1.5 Tesla," *J Magn. Reson. Imaging*, Vol. 15, No. 3, 241–250, 2002.

2. Dormont, D., P. Cornu, B. Pidoux, et al., "Chronic thalamic stimulation with three-dimensional MR stereotactic guidance," *Am. J. Neuroradiology*, Vol. 18, No. 6, 1093–1097, 1997.

3. Nyenhuis, J. A., S. M. Park, et al., "MRI and implanted medical devices: Basic interactions with an emphasis on heating," *IEEE Trans. Device and Materials Reliability*, Vol. 5, No. 3, 467–480, 2005.

4. Jin, J. M., J. Chen, W. C. Chew, et al., "Computation of electromagnetic fields for high-frequency magnetic resonance imaging applications," *Phys. Med. Biol.*, Vol. 41, 2719–2738, 1996.

5. Nitz, W. R., A. Oppelt, W. Renz, et al., "On the heating of linear conductive structures as guide wires and catheters in interventional MRI," *J. Magn. Reson. Imag.*, Vol. 13, No. 1, 105–114, 2001.

6. Nguyen, U. D., J. S. Brown, et al., "Numerical evaluation of heating of the human head due to magnetic resonance imaging," *IEEE Trans. Biomed. Eng.*, Vol. 51, No. 8, 1301–1309, 2004.

7. King, R. W. P., B. S. Trembly, and J. W. Strohbehn, "The electromagnetic field of an insulated antenna in a conducting or dielectric medium," *IEEE Trans. MTT*, Vol. 31, No. 7, 574–583, 1983.

8. King, R. W. P., "Antennas in material media near boundaries with application to communication and geophysical exploration, Part I: The bare metal dipole," *IEEE Trans. on Anten. and Prop.*, Vol. 34, No. 4, 483–489, 1986.

9. King, R. W. P., "Antennas in material media near boundaries with application to communication and geophysical exploration,

Part II: The terminated insulated antenna," *IEEE Trans. on Anten. and Prop.*, Vol. 34, No. 4, 490–496, 1986.

10. Atlamazoglou, P. E. and N. K. Uzunoglu, "Galerkin moment method for the analysis of an insulated antenna in a dissipative dielectric medium," *IEEE Trans. MTT*, Vol. 44, No. 7, 988–996, 1998.

11. Park, S. M., R. Kamondetdacha, A. Amjad, and J. A. Nyenhuis, "MRI safety: RF induced heating on straight wires," *IEEE Trans. Magn.*, Vol. 41, No. 10, 4197–4199, 2005.

12. Volakis, J. L., A. Chatterjee, and L. C. Kempel, "Review of the finite-element method for three-dimensional electromagnetic scattering," *J. Opt. Soc. Am. A*, Vol. 11, No. 4, 1422–1433, 1994.

13. Jin, J. M., *The Finite Element Method in Electromagnetics*, 2nd edition, John Wiley and Sons, 2002.

14. Park, S. M., Ph.D. thesis, Purdue University, West Lafayette, IN, 2006.

15. Ibrahiem, A., C. Dale, W. Tabbara, and J. Wiart, "Analysis of the temperature increase linked to the power induced by RF source," *Progress In Electromagnetics Research*, PIER 52, 23–46, 2005.

16. Kuo, L.-C., Y.-C. Kan, and H.-R. Chuang, "Analusis of a 900/1800-Mhz dual-band gap loop antenna on a handset with proximate head and hand model," *J. of Electromagn. Waves and Appl.*, Vol 21, No. 1, 107–122, 2007.

17. Khalatbari, S., D. Sardari, A. A. Mirzaee, and H. A. Sadafi, "Calculating SAR in two models of the human head exposed to mobile phones radiations at 900 and 1800 MHz," *Progress In Electromagnetics Research Symposium*, 104–109, Cambridge, USA, March 26–29, 2006.

18. Kouveliotis, K. and C. N. Capsalis, "Prediction of the SAR level induced in a dielectric sphere by a thin wire dipole antenna," *Progress In Electromagnetics Research*, PIER 80, 321–336, 2008.